Author Manuscript

Author Manuscript

Author Manuscript

Author Manuscript

HHS Public Access

Author manuscript

Ultrasound Med Biol. Author manuscript; available in PMC 2021 December 01.

Published in final edited form as:

Ultrasound Med Biol. 2020 December ; 46(12): 3426–3439. doi:10.1016/j.ultrasmedbio.2020.08.022.

Multiparametric Ultrasound for Targeting Prostate Cancer: Combining ARFI, SWEI, QUS, and B-mode

D. Cody Morris[a,*], **Derek Y. Chan**[a], **Theresa H. Lye**[b], **Hong Chen**[b], **Mark L. Palmeri**[a], **Thomas J. Polascik**[c], **Wen-Chi Foo**[d], **Jiaoti Huang**[d], **Jonathan Mamou**[b], **Kathryn R. Nightingale**[a]

[a]Department of Biomedical Engineering, Duke University, Durham, NC, USA

[b]Lizzi Center for Biomedical Engineering, Riverside Research, New York, NY, USA

[c]Department of Surgery, Duke University Medical Center, Durham, NC, USA

[d]Department of Pathology, Duke University Medical Center, Durham, NC, USA

Abstract

Diagnosing prostate cancer (PCa) through standard transrectal ultrasound (TRUS) guided biopsy is challenging due to the sensitivity and specificity limitations of B-mode imaging. We used a linear support vector machine (SVM) to combine standard TRUS imaging data with acoustic radiation force impulse (ARFI) imaging data, shear wave elasticity imaging (SWEI) data and quantitative ultrasound (QUS) midband fit (MF) data to enhance lesion contrast into a synthesized multiparametric ultrasound (mpUS) volume. This SVM was trained and validated using a subset of 20 patients and tested on a second subset of 10 patients. mpUS led to a statistically significant improvement in contrast, contrast-to-noise ratio (CNR), and generalized CNR (gCNR) when compared to standard TRUS B-mode and SWEI; contrast and CNR when compared to MF; and CNR when compared with ARFI. ARFI, MF, and SWEI also outperformed TRUS B-mode in contrast, with MF outperforming B-mode in CNR and gCNR as well. ARFI, while only yielding statistically significant differences in contrast compared to TRUS B- mode, captured critical qualitative features for lesion identification. MpUS enhanced lesion visibility metrics and is a promising technique for targeted TRUS-guided prostate biopsy in the future.

Keywords

Prostate Cancer; Multiparametric Ultrasound; Elasticity Imaging; Acoustic Radiation Force Impulse Imaging; Shear Wave Elasticity Imaging; Mid-band Fit

Introduction

Prostate cancer (PCa) is the leading cause of new cancer diagnoses and the second leading cause of cancer related death for men living in the United States (Siegel et al., 2020). There

*Corresponding Author: D. Cody Morris, Room 1427, Fitzpatrick Center (FCIEMAS), 101 Science Drive, Campus Box 90281, Durham, NC 27708-0281; cody.morris@duke.edu; Phone, 919-660-5223.

Conflict of Interest

Authors K. Nightingale and M. Palmeri have intellectual property related to radiation force-based imaging technologies that has been licensed to Siemens, Samsung, and MicroElastic Ultrasound Systems.

Author Manuscript Author Manuscript Author Manuscript Author Manuscript

will be an estimated 191,930 new cancer diagnoses and 33,330 deaths in the United States in 2020 related to PCa (Siegel et al., 2020). The gold standard approach for diagnosing PCa is through transrectal ultrasound (TRUS) guided biopsy following an elevated prostate-specific-antigen (PSA) test or a suspicious digital rectal exam (DRE). TRUS guided biopsy typically consists of 10–12 biopsy cores sampled systematically throughout the prostate where ultrasound is used to ensure the location of the biopsy needle remains within the prostate (Mottet et al., 2017). Studies report TRUS guided biopsy sensitivities and specificities ranging from 39–75% and 40–82%, respectively (Postema et al., 2015; Heijmink et al., 2011). These poor sensitivities and specificities are expected as approximately 55% of PCa is hypoechoic, 40% is isoechoic, and 5% is hyperechoic (Heijmink et al., 2011). This lack of targeting in TRUS guided biopsy along with the limited sensitivity, specificity, and lesion contrast in TRUS B-mode imaging leads to only 18–36% of men suspected of having PCa being diagnosed following the results of their first biopsy (Elabbady and Khedr, 2006).

To alleviate the limitations of TRUS guided biopsy, standard TRUS B- mode can be combined with additional imaging methods which have increased contrast for PCa to improve lesion detectability. Two techniques which are currently being explored are multiparametric magnetic resonance imaging (mp-MRI) fusion and contrast enhanced ultrasound (CEUS). mp- MRI TRUS fusion consists of registering an mp-MRI scan of the patient's prostate with live B-mode during biopsy for PCa targeting. mp-MRI TRUS fusion biopsy results in increased sensitivity of 85–93% and specificity of 41–49% (Ahmed et al., 2017; Siddiqui et al., 2015). CEUS consists of injecting microbubbles before TRUS B-mode imaging and examining the bubble dynamics as they perfuse through the prostate. CEUS leads to an increase in lesion detection as the enhanced visibility of the vasculature for PCa is different from healthy prostatic tissue corresponding to a sensitivity of 73% and specificity of 58% (Halpern, 2006; Postema et al., 2016). However, these two methods come with drawbacks as mp-MRI requires increased resources and additional physician time and CEUS requires injection of a contrast agent.

Other techniques which do not rely on additional resources to enhance lesion contrast are acoustic radiation force impulse (ARFI) imaging and shear wave elasticity imaging (SWEI) which are elasticity-based, and quantitative ultrasound (QUS) methods based on the spectral content of the backscattered ultrasound signals (Doherty et al., 2013; Feleppa et al., 2011). ARFI and SWEI use acoustic radiation force (ARF) to mechanically displace the tissue and assess its elastic properties. ARFI is currently being investigated as a technique for identifying PCa *in vivo* and has been demonstrated to identify 71% of clinically significant PCa with a positive predictive value of 95% (Palmeri et al., 2016). ARFI images reflect a relative measure of tissue stiffness. SWEI, in contrast, provides a quantitative estimate of tissue stiffness which may be relevant to identifying PCa and its clinical stage (Barr et al., 2012; Rosenzweig et al., 2012; Rouviere et al., 2017; Wei et al., 2018). Supersonic Imagine has recently developed a TRUS SWEI system which has been reported to differentiate between PCa and benign prostate tissue *in vivo*, but its diagnostic capability has yet to be demonstrated through prospective studies (Rouviere et al., 2017). Spectral-based QUS methods quantify the scattering properties of tissues by computing normalized spectra. The normalized spectra are fit to several models to generate multiple parameters which are then

Author Manuscript Author Manuscript Author Manuscript Author Manuscript

analyzed using classifiers, neural networks, or alternate machine learning methods. When used to identify PCa, QUS algorithms result in an elevated area under the receiver operator characteristic curve (AUC) of 0.844 ± 0.018 compared to the standard TRUS B-mode imaging AUC of 0.638 ± 0.031 (Feleppa et al., 2011; Oelze and Mamou, 2016). Midband fit (MF) is one of the most common parameters in QUS analyses and is generated using a linear fit to the normalized backscattered spectra (Oelze and Mamou, 2016; Lizzi et al., 1983).

We have obtained matched 3-D ARFI, SWEI, MF, and TRUS B-mode data *in vivo* in 35 patients expecting radical prostatectomy in an institutional review board (IRB) approved study. We explore several classifiers and use them to synthesize a multiparametric ultrasound (mpUS) image volume combining information from these ARFI, SWEI, MF, and B-mode data. We calculate the contrast, contrast-to-noise ratio (CNR), and generalized CNR (gCNR), for the individual data volumes along with the summed mpUS data of PCa lesions as determined from the corresponding whole mount histology data. The goal of this work is to determine the feasibility of using mpUS to provide imaging guidance for targeted needle prostate biopsy.

Materials and Methods

Data Acquisition

3D ARFI, SWEI, midband fit (MF) and B-mode data were acquired in 35 patients with biopsy-confirmed PCa. These patients provided written informed consent and were imaged in an IRB-approved study immediately preceding radical prostatectomy. During data acquisition, patients were in a supine position with legs supported by stirrups and under general anesthesia. Data were acquired using a modified Siemens SC2000 Scanner (Siemens Medical Solutions, Issaquah, WA USA) and either an ACUSON ER7B or a custom designed Siemens 12L4 transrectal ultrasound probe. These side-fire transrectal probes were paired with a modified CIVCO Micro-Touch stabilizer and rotation stage (CIVCO Medical Solutions, Kalona, IA USA) to acquire 100 sagittal images of the prostate at an angular spacing of 1–1.5 degrees. The rotation stage was modified with a stepper motor and optical sensor to automatically control the rotation of the transducer (Palmeri et al., 2016). The entire volume of the prostate was angularly traversed twice, with the patient-right to left acquisition corresponding to a combined ARFI and SWEI sequence and the patient-left to right rotation corresponding to a high-quality MF and B-mode acquisition. The entire data acquisition took approximately 14 minutes per patient. After each data set was processed, they were scan converted and visualized in 3-D Slicer with a $0.15 \times 0.15 \times 0.15$ mm^3 voxel size (Fedorov et al., 2012). As the transducer is not manually adjusted during the data acquisition, the ARFI, SWEI, MF, and B-mode data can be co-localized into common imaging planes following scan conversion. 20 patients were imaged with the ER7B and 15 patients were imaged with the 12L4. The data from these patients were divided into training and testing subsets (Figure 1).

The ARFI and SWEI combined sequence excitation and tracking parameters used in this study are summarized in Tables 1 and 2. For the ER7B transducer, this sequence was previously described by Palmeri et al. (Palmeri et al., 2016). To summarize the sequences, a three focus multi-focal-zone combined ARFI push excitation was used to generate ARFI

Author Manuscript Author Manuscript Author Manuscript Author Manuscript

displacements with an elongated depth of field Rosenzweig et al. (2015). Tracking was performed with 16:1 parallel receive with four track beams placed inside the beam width (0.17 mm spacing) of the push excitation to measure the ARFI displacements (Figure 2). The remaining twelve tracking beams were split into two groups of six tracking beams which were positioned to the left and right of the push excitation to measure the shear wave propagation. For each group of 6, the tracking beams were laterally offset from the push and spaced approximately one beamwidth (0.76 or 0.78 mm) apart (Figure 2) (Rosenzweig et al., 2012). The 16 tracking lines were repeated for 4–5 ms at a PRF of 8 or 10 kHz to acquire in-phase and quadrature (IQ) data through time. The ARFI push and corresponding 16 track lines ensemble was repeated 82 times across the face of the transducer to create a 55 mm lateral field of view.

Data Processing

ARFI/SWEI Processing: Loupas' phase shift estimator was used on the acquired IQ data from the ARFI and SWEI combined sequence to calculate particle velocity progressively through time with a correlation coefficient threshold of 0.98 applied to the estimates at each time step (Loupas et al., 1995). This progressively tracked particle velocity was integrated through time to calculate the displacement through time profile for the ARFI data volume. Depth dependent gain and histogram equalization were also applied to this ARFI data to account for attenuation and focal effects, and enhance lesion contrast, respectively (Palmeri et al., 2015).

Shear wave speeds were calculated from the estimated particle velocities from the off axis tracking lines using techniques described by Manduca et al. (Manduca et al., 2003), Lipman et al. (Lipman et al., 2016), Song et al. (Song et al., 2014), and Chan et al. (Chan et al., 2018). These data were low pass filtered using a phase-preserving 2^{nd} order Butterworth filter with a cutoff frequency of 1.5 kHz. 3D directional filtering was performed to limit the impact of reflected waves (Lipman et al., 2016) and correlation based 2D vector tracking was used to more accurately estimate the shear wave speeds at each location (Song et al., 2014). Finally, overlapping shear wave tracking locations from neighboring ARFI ensembles were averaged to decrease the noise on each individual shear wave speed estimate and estimates greater than 12 m/s or with correlation coefficients lower than 0.7 were discarded (Chan et al., 2018).

B-mode Processing: The high-quality B-mode acquisition consisted of 126 focused transmits which spanned the 55 mm field of view with 7:1 parallel receive tracking and coherent beamforming. For both transducers, a tracking and B-mode imaging transmit configuration with a 7.0 MHz center frequency and an F/3 focal configuration was used with an F/1 dynamic receive configuration (Palmeri et al., 2016). These B-mode data were processed by log compressing and applying axial and lateral median filters.

QUS Processing: Prior to the calculation of MF, each B-mode (i.e., IQ) data volume was remodulated to a 56 MHz sampling frequency radiofrequency data volume. The MF was then calculated within 3D, overlapping regions of interest (ROIs) that spanned the entirety of each RF data volume using standard QUS methods (Oelze and Mamou, 2016). Each ROI

Author Manuscript Author Manuscript Author Manuscript Author Manuscript

had an axial length of 1.75 mm and lateral length of 0.64 mm. The ROI length in the elevational dimension typically ranged from 1.22 mm for small prostates at shallow axial depths to 6.41 mm for large prostates at the maximum depth used for analysis. A 60% lateral and elevational overlap and 80% axial overlap were used. After the entire MF volume was computed, the MF data were then interpolated to 99% lateral and elevational overlap and 98% axial overlap to generate a high-resolution MF volume.

Within each ROI, the MF was extracted from a linear fit to the ROI's backscatter coefficient (BSC), where the BSC was computed by the reference- phantom method (Rohrbach et al., 2018; Yao et al., 1990). Linear attenuation compensation was used for the prostate tissue and phantom with an assumed value of 0.5 dB/MHz/cm. An affine attenuation model was used for the QUS reference phantom with a measured value of 0.55 dB/MHz/cm - 1.0 dB/cm. The QUS reference phantom consisted of agarose, propylene glycol, and Germall Plus (International Specialty Products, Wayne, NJ) with 60 μm diameter glass beads and a 25 μm thick Saran Wrap surface membrane (Saran Wrap; Dow Chemical, Midland, MI). The glass beads had a speed of sound of 5570 m/s, mass density of 2.38 g/cm^3, Poisson's ratio of 0.21, and scatterer number density of 46.7 beads/mm^3. The transmission through the Saran Wrap was compensated using a speed of sound of 2400 m/s, acoustic impedance of 4.1 MRayl in the Saran Wrap, and an acoustic impedance of 1.5 MRayl in the reference phantom and in water.

After the computation of the BSC, a linear fit to the BSC was obtained within a adaptive bandwidth for each ROI which was estimated at 12 dB above the noise plateau; the noise plateau was calculated within 0.7 – 1.2 MHz. Afterwards, the MF was determined as the value of the fitted line to the BSC at 5 MHz.

Histology

Immediately following imaging, prostates were radically excised and whole mounted. The slides were stained with hematoxylin and eosin (H&E) for pathological analysis. The prostates were sliced every 3 mm from the apex to base and examined by board-certified pathologists who identified locations and Gleason Grade Group of the PCa foci along with regions of benign prostate hyperplasia (BPH), and atrophy. An identified lesion was considered clinically significant if its Gleason Grade Group was greater than or equal to 2 (Gleason Score 3+4=7) or was larger than 0.5 mL (Weinreb et al., 2016; Epstein et al., 2016). As in the work by Palmeri et *al.,* the histology slides were not registered with the ARFI, SWEI, MF, and B-mode data due to the slice thickness and potential for error in the slice orientation (Palmeri et al., 2015, 2016). Instead, the prostate 27-region model was used to localize the center for each lesion, which was then used to identify PCa in the imaging volumes (Dickinson et al., 2011). An Epson 750 Pro scanner (Epson America, Long Beach, CA, USA) was used to scan the histology slides individually and the slides were stacked to create a histology volume. Volumes of PCa foci were calculated as ellipsoids using triaxial measurements made by the pathologists.

Author Manuscript Author Manuscript Author Manuscript Author Manuscript

PCa Identification and Classifier Training

For patients imaged using the ER7B and 12L4 transducers (Figure 1), the index lesion and a healthy region were identified and segmented in ARFI, SWEI, MF, and B-mode data volumes using 3D Slicer (Fedorov et al., 2012). These regions were identified by the authors after visually aligning the histologically determined ground truth locations in the pathology volumes with the PCa contrast provided in each volume. Healthy regions were conservatively segmented and restricted to regions that were opposite the PCa, within the peripheral zone (PZ), and did not contain atrophy, calcifications, or BPH. The intersection of the individual segmentations from each modality were used to identify PCa and healthy tissue. Five 12L4 patients had diffuse PCa and were excluded in this step because a healthy region could not be confidently identified. Table 3 contains the Gleason Grade Groups for the ER7B and 12L4 patients.

The resulting distributions of 980,620 training voxels from the segmented regions of the ER7B cases were normalized to have a zero mean and unit standard deviation for further classifier analysis. Four classifiers: Linear Discriminant Analysis (LDA), linear Support Vector Machines (SVM), Decision Trees, and Random Forests, were chosen for their ease of implementation and simplicity and were used to examine the combination of ARFI, SWEI, MF, and B-mode. Scikit-learn (scikit-learn.org) version 0.23.1 (Pedregosa et al., 2011)was used to implement these four classifiers with slight modifications made to the default hyperparameters: the LDA's tolerance was set to 1E-4, the SVM's tolerance was set to 1E-6, and the Random Forest used 10 estimators. Of the 20 ER7B cases used in training, only 15 had a region of the prostate which could be identified as healthy tissue. Therefore, 15-fold cross validation was performed on the classifiers where, in each fold, a single patient's healthy and PCa voxels were excluded from training and used to assess the performance of the classifier. The classifier performance was validated by generating the mpUS volume as specified by the classifier and calculating the contrast, CNR, and gCNR between the PCa and healthy region in both the mpUS volume and the individual data volumes. The classifier which yielded the highest contrast, CNR, and gCNR was selected to combine the ARFI, SWEI, MF, and B-mode data into an mpUS data volume for the subsequent 12L4 test data.

Contrast, CNR, and gCNR

Contrast and CNR are two commonly used lesion visibility metrics (Smith et al., 1985; Patterson and Foster, 1983). In Eqns. 1–3, μ_h and μ_p represent the means and σ_h and σ_p represent the standard deviations of the voxels in the healthy and PCa segmentations, respectively. Eqn. 1 is applied to the ARFI, B-mode, and MF data as the values associated with PCa are typically lower than the values associated with healthy tissue because the majority of PCa is hypoechoic and in ARFI images regions of increased stiffness appear darker. Eqn. 2 is used for the SWEI and mpUS data because PCa is stiffer than healthy tissue which corresponds to increased voxel values in SWEI and increased suspicion in mpUS. Two different equations (Eqns. 1, 2) are used to compute contrast to keep the relative contrast consistent across modalities. Contrast can be heavily affected by any dynamic range adjustments, such as the histogram equalization applied to the ARFI data before visualization or the colorbar inversion applied to SWEI and mpUS. Only one equation is used to compute CNR (Eqn. 3) because CNR accounts for the noise in an image and is

Author Manuscript Author Manuscript Author Manuscript Author Manuscript

consistent whether PCa corresponds to elevated or suppressed values compared to healthy tissue.

$$Contrast_{A,B,MF} = \frac{\mu_h}{\mu_p} \tag{1}$$

$$Contrast_{S,Mp} = \frac{\mu_p}{\mu_h} \tag{2}$$

$$CNR = \frac{|\mu_p - \mu_h|}{\sqrt{\sigma_p^2 + \sigma_h^2}} \tag{3}$$

gCNR is a metric which assesses the overlap in the distributions of the two regions of interest and is designed to be robust to dynamic range adjustments (Rodriguez-Molares et al., 2020). In Eqn. 4, p_p and p_h represent the probability distribution for the PCa and healthy segmentations, respectively. Therefore, gCNR is always between 0 and 1 and a value of 1 represents no overlap between the two distributions and a value of 0 represents complete overlap. Figure 3 is included as an example where the gCNR of the overlapping regions of P_p and P_h probability distributions (OVL) would be subtracted from 1 to generate the gCNR. gCNR is a measure of how separable the two regions would be by a computer whereas contrast and CNR are more related to how separable the regions would be to a human eye.

$$gCNR = 1 - \int \min\{p_p(x), p_h(x)\}dx \tag{4}$$

Phantom Validation

After classifier validation, the weightings of the optimal classifier were used to combine data from a custom prostate phantom to assess performance of mpUS in a known entity. This phantom is a custom Zerdine® CIRS (CIRS Inc., Norfolk VA, USA) phantom designed to emulate the prostate PZ and central zone (CZ) and has 6 lesions of varying Young's Modulus (E), echogenicity, and size, with properties as shown in Table 4. With the PZ as the reference, contrast, CNR, and gCNR were calculated for each of the 6 lesions and the transition zone (TZ) in ARFI, SWEI, B-mode, MF, and mpUS. The lesion definitions are included in Figure 4.

Classifier Testing and Statistical Analysis

The optimal classifier was then used to create mpUS volumes from the 10 patients who were imaged with the 12L4 transducer (i.e., the test data). The Gleason Grade Groups for the 12L4 test patients are included in Table 3. The potential locations, sizes, and Grade Groups are an appropriate representation of the training set. As with the training data, PCa lesions and healthy regions were segmented, and the corresponding 2,097,042 voxels were extracted (Fedorov et al., 2012). Contrast, CNR, and gCNR were calculated for each patient and a two-way analysis of variance (ANOVA) with repeated measures was performed to examine

Author Manuscript Author Manuscript Author Manuscript Author Manuscript

the differences between modality (ARFI, B-mode, MF, SWEI, and mpUS), and metric (Contrast, CNR, and gCNR). Further repeated measures ANOVAs were performed for each metric to examine the relationship between the modalities, and paired t-tests were used to determine which specific modalities provide improved performance. Bonferroni correction was applied to the paired t-tests to reduce the family-wise error rate, bringing the significant p-value from $p<0.05$ to $p<0.005$.

Results

Table 5 contains the lesion visibility metrics calculated using the segmented PCa and healthy regions in 15 ER7B training patients. ARFI and SWEI perform nearly the same, and yield the largest mean contrast and CNR, followed by MF. The three lesion visibility metrics obtained from B- mode had lower means compared to ARFI, SWEI, and MF.

The classifier validation contrast, CNR, and gCNR are included in Table 6. These values represent the mean ± standard deviation of the 15-fold cross validation. The LDA, SVM, and Random Forest yield comparable performance in CNR and gCNR, though the Random Forest suffers in contrast. The Linear SVM was chosen for the remainder of the analysis as all classifiers were comparable but the SVM yielded a slightly higher CNR and contrast, and yielded the simple combination (Eqn. 5) of modalities to generate the mpUS data volume, where mpUS represents the combined image, and A,B,S, and MF represent the ARFI, B-mode, SWEI, and mid-band fit volumes, respectively.

$$mpUS = -1.6\mathrm{A} - 1.0\mathrm{B} + 3.6\mathrm{S} - 3.4\mathrm{MF} \quad (5)$$

Figure 5 includes sample axial (subfigures A-E) and coronal (subfigures F-J) images from the custom prostate phantom demonstrating the visibility of various inclusions listed in Table 4. In this image, dark regions correspond to low tissue displacement (ARFI), high shear wave speeds (SWEI), low echogenicity (B-mode), low backscatter (MF), and higher suspicion (mpUS). Note the hyperechoic regions in the B-mode and MF images corresponding to Lesion 1 (green arrows) and the TZ (blue arrows). As mentioned in Table 4, Lesion 1 and the TZ are hyperechoic compared to the PZ but still have stiffness contrast leading to Lesion 1 and the TZ being easily visible in ARFI, SWEI, and mpUS but difficult to visualize in B-mode and MF. Additionally, the hypoechoic region at depth in B-mode (C) corresponds with regions of poor signal-to-noise ratio (SNR) in ARFI (A) and SWEI (B) due to poor motion tracking in regions with poor B-mode SNR as predicted by the Cramer-Rao Lower Bound (Walker and Trahey, 1995; Byram et al., 2013).

Figure 6 shows the contrast (A), CNR (B), and gCNR (C) of the custom prostate phantom inclusions. Subfigure A demonstrates decreased contrast in B-mode and MF and decreased mpUS values corresponding to the hyperechoic inclusions (TZ and L1). All three subfigures demonstrate how mpUS consistently performs well compared to the individual modalities and how B-mode consistently performs poorly across all metrics.

Axial images from a representative test patient are shown in Figure 7. A clinically significant 4.2 mL Gleason Grade Group 4 (Gleason Score 4+4=8) lesion is identified in

Author Manuscript Author Manuscript Author Manuscript Author Manuscript

histology (A) and segmented in ARFI (B), SWEI (C), B-mode (D), and MF (E) in purple. Healthy regions are indicated in subfigures B-E in light blue. The mpUS image (F) demonstrates the intersections for both the healthy (dark blue) and PCa (pink) segmentations. The capsule (green outline) and CZ (red outline) are included to signify the prostate anatomy. In the following patient images, colorbars have been selected to portray cancer as darker than benign tissue (low echogenicity, backscatter, and diplacement, and higher shear wave speeds and mpUS levels of suspicion all appear darker than other tissues). Note the slight differences in shape of the segmented contrasting regions of PCa in each imaging modality.

Figure 8 includes axial images from an additional test patient. A clinically significant 1.0 mL Gleason Grade Group 3 (Gleason Score 4+3=7) lesion is identified in histology (A) and segmented in ARFI (B), SWEI (C), B-mode (D), and MF (E) in purple. Healthy regions are once again indicated in subfigures B-E in light blue. The mpUS image (F) demonstrates the intersections for both the healthy (dark blue) and PCa (pink) segmentations. This patient includes a common imaging artifact produced by the presence of calcifications (green arrows). Subfigures B,D,E, and F are impacted by the presence of the calcifications with bright spots appearing inside the central zone. Note that SWEI (C) and ARFI (B) are both masked in the regions deep to the calcifications due to the lack of signal there (having failed the correlation coefficient thresholding for displacement estimation).

Axial images from a final test patient are shown in Figure 9. A clinically significant 5.3 mL Gleason Grade Group 2 (Gleason Score 3+4=7) lesion is identified in histology (A) and segmented in ARFI (B), SWEI (C), B-mode (D), and MF (E) in purple. A healthy region is indicated in subfigures B-E in light blue. The mpUS image (F) demonstrates the intersections for both the healthy (dark blue) and PCa (pink) segmentations. This example, once again, shows representative shape differences in the suspicious region based on the imaging modality. The PCa in ARFI (B) has a considerably different shape compared to the PCa identified in SWEI (C), B-mode (D), and MF (E). Also note the limited signal quality of SWEI at depth due to poor motion tracking SNR.

Table 7 includes the results from the two-way repeated measures ANOVA indicating that both the metric (contrast, CNR, and gCNR) and modality (ARFI, B-mode, SWEI, MF, and mpUS) significantly explain differences in the data. Table 8 includes the results from three repeated measures ANOVAs, one for each metric which examined the variance explained by the differences in modality. In all three cases, modality was a contributing factor to the variance ($p<0.0001$ for each metric).

Figure 10 shows the contrast (A), CNR (B), and gCNR (C) of the PCa lesions from the 10 12L4 test patients. mpUS (red triangle) significantly outperforms B-mode and SWEI in contrast, CNR, and gCNR (all pairwise tests have $p<0.0039$) and also results in improved contrast and CNR compared to MF (all pairwise tests have $p<0.0028$) and improved CNR compared to ARFI ($p=0.0007$). MF results in better performance in all metrics compared to B-mode (all pairwise tests have $p<0.0006$). ARFI and SWEI also have better contrast than B-mode ($p=0.0017$). Results from the paired T-tests are included in Table 9.

Author Manuscript Author Manuscript Author Manuscript Author Manuscript

Discussion

The mpUS approach takes advantage of multiple mechanisms of contrast available in ultrasonic prostate images: backscatter and elasticity. As such, an improvement in cancer visualization is expected. However, each modality also has limitations. Both ARFI and SWEI image the elasticity of a tissue, but the reliability of the measurements decreases as the tissue stiffness increases. Additionally, both ARFI and SWEI suffer at depth due to energy penetration limitations, with SWEI being further limited by the radial decay of energy away from the ARF axis. TRUS B-mode imaging is limited in both sensitivity and specificity due to 40% of PCa being isoechoic (Postema et al., 2015; Heijmink et al., 2011). MF is also limited in these cases because it generally trends with B-mode image brightness even though it is rigorously corrected for attenuation, field properties, and system settings. Due to these limitations, a combined approach has the potential to enhance lesion visibility by combining complementary information from additional modalities to mitigate potential pitfalls of any individual modality.

In the 15 ER7B patients that were used for classifier validation, all metrics demonstrated traditional B-mode lesion visibility performing the worst (Table 5). The heightened contrast, CNR, and gCNR in ARFI, SWEI, and MF compared to B-mode is encouraging as each of these modalities was developed to enhance lesion visibility in scenarios where B-mode fails.

When combining ARFI, SWEI, B-mode, and MF into a single mpUS image, the general trend was an increase in CNR and gCNR compared to each individual modality (Tables 5 and 6). This finding indicates that each modality contains some amount of unique information. There is also a decrease in contrast between ARFI and SWEI's individual data compared to the mpUS volume (Tables 5 and 6) which is caused by the scaling of the data when combined by the classifier.

The four investigated classifiers yielded comparable contrasts, CNR, and gCNR, though the linear SVM with SGD was chosen for the subsequent analyses as it yielded high contrast and CNR and comparable gCNR to the LDA and random forest algorithm. This linear SVM combined ARFI, B-mode, SWEI, and MF using the expression in Eqn. 5. As the data from the four imaging techniques were normalized to zero mean and unit standard deviation, the absolute value of the scale factors applied in the linear SVM, shown in Eqn. 5, relate to the approximate contribution of the individual modality.

For example, SWEI is approximately twice as influential when compared to ARFI. The signs applied to each scalar are due to the relative contrast of PCa to healthy tissue in each imaging modality. As PCa is typically stiffer than healthy PZ, lesions lead to lower values in ARFI and higher values in SWEI. The lower values in ARFI correspond to a decrease in displacement and the higher values in SWEI correspond to an increased shear wave speed. Both changes are indicative of increased stiffness.

SWEI is approximately twice as influential as ARFI in the SVM combination because the range of values identified as PCa or healthy overlap more in ARFI than they do in SWEI. This is caused by the histogram equalization applied to ARFI. In ARFI, the voxels which appear to be misclassified are stretched further from the class mean, thus weakening ARFI

Author Manuscript Author Manuscript Author Manuscript Author Manuscript

to the SVM. Additionally, during SWEI processing several estimates are used to obtain the value at a single voxel which suppresses the variability of the voxels which appear to be misclassified and thus strengthens SWEI to the SVM. It is interesting to note that the difference in classifier weighting between ARFI and SWEI cannot be explained by counting the number of voxels which overlap as the gCNR values (Table 5) indicate that the number of overlapping voxels are approximately equal. Additionally, B-mode is the least influential of the modalities. This is expected as B-mode's contrast, CNR, and gCNR (Table 5) also demonstrate the least separation between the regions identified as PCa and healthy.

Applying the linear SVM combination to the custom designed prostate phantom allowed for a confidence-building assessment of how contrast, CNR, and gCNR may change with modality (ARFI, SWEI, B-mode, MF, and mpUS) in a known material (Table 4). In Figure 5, two structures (TZ (blue arrows) and L1 (green arrows)) are present which are hyperechoic and have relatively low B-mode and MF contrast. Due to the enhanced elastic contrast in ARFI (A and F) and SWEI (B and G), the inclusions are readily apparent in the mpUS images E and J.

The hyperechoic B-mode appearance of L1 and the TZ was associated with decreased contrast in the mpUS images (Fig 4A). When training the classifier, none of the lesions included were hyperechoic as they only account for 5% of PCa, which leads to this poor performance in this subset of inclusions (Heijmink et al., 2011). For the hypoechoic inclusions (L2-L6), mpUS performs as expected, either performing as well or better than the individual modalities.

The CNR values in Figure 6B follow the trend predicted by the phantom material (Table 4). Inclusions L4, L5, and L6 were extremely noisy in the elasticity metrics due to their elevated stiffnesses (Table 4), and positions within the phantom, either being particularly far from the face of the transducer or close to other inclusions which may have induced wave reflections and interference which were difficult to assess with current processing. This added noise led to a decrease in the ARFI and, more notably, the SWEI CNR.

In examining the gCNR values for the phantom analysis (Figure 6C), the ARFI and SWEI gCNRs both decrease as the Young's Modulus increases, due to an increase in the noise measured in the lesion which then increases the amount of overlap of the probability distributions. This is opposite the expected trend based upon the increased stiffness contrast in these lesions. The MF and B-mode gCNRs follow eachother, with MF being consistently higher. This trend is expected to some extent because MF quantifies the amount of energy bacskcattered by the tissue in a system- and user-independent fashion.

Additionally, the mpUS gCNR is consistently above 0.9, even for the inclusions where ARFI, SWEI, B-mode, or MF gCNR drop below 0.9. This indicates that in a clinical setting, where potentially only one imaging volume can be assessed by a urologist, mpUS would provide the most consistent results.

Three image volumes from the test patients are included in Figures 7–9. In each of these cases, the lesion shape and size appeared different in each modality, with the case with the largest differences appearing in Figure 9B and C. These shape and size differences may be

Author Manuscript Author Manuscript Author Manuscript Author Manuscript

related to shear wave reflection artifacts and SNR limitations leading to differences between ARFI and SWEI. Shear wave reflection artifacts appear as additional signal in the particle velocity curve at a later time than the true shear wave and can result in slower shear wave speed estimates at the edges of PCa lesions (Lipman et al., 2016). The apparent lesion shape change supports the use of mpUS, as regions which appear suspicious in mpUS correspond to overlapping regions of suspicion in the combined modalities.

The lesion shape and size difference across modalities was also a contributing factor in our decision to use the intersection of the suspicious regions in each modality to train and assess mpUS. This intersection is a conservative estimate of the PCa and captures approximately 17% of the ARFI, 34% of the B-mode, 32% of the MF, and 33% of the SWEI segmentations. While using the intersection ensured we assessed only voxels which were PCa, it also artificially inflates the performance of MF and SWEI in cases where only a small portion of the PCa is identified when compared to histology and to ARFI (Figure 7 (E) and Figure 9 (C & E)). This inflation leads to increased weightings for MF and SWEI in the classifier (Eqn. 5) and possibly biases the lesion visibility metrics for MF and SWEI.

While the intersection approach is not perfect, an additional benefit is that the spatial resolution differences across modalities does not impact the contrast, CNR, or gCNR. Using the intersection of the segmentations captures the center of the PCa (ideal for targeted biopsy) but misses the border where the spatial resolution differences between the elasticity modalities and B-mode and MF could impact the visibility metrics.

Historically, border definition, regional contrast, and texture have been important features employed to assign suspicion scores for PCa (index of suspicion) when reading ARFI volumes (Palmeri et al., 2016). Using the lesion visibility metrics applied to the voxels within the intersection of the segmented regions is a more objective approach though it removes qualities a reader would use to identify a suspicious region. While ARFI only statistically outperformed B-mode in contrast, it clearly outperforms the other modalities in Figures 7 and 9 when considering the border delineation, local regional contrast and texture. ARFI also more accurately represents the size and shape of the lesion identified by histology in both figures. Additionally, in Figure 8, the lesion size and shape is relatively constant across modalities which leads to mpUS capturing the qualitative features used for lesion detection along with performing well quantitatively.

Two specific limitations are made clear in the included test patients. Figure 8 demonstrates calcifications (green arrows) which limit the ability of any ultrasound modality to detect PCa beneath the calcifications as they block the sound propagation, and Figures 7 and 9 both demonstrate poor SWEI (and ARFI) SNR at depth. As with conventional ultrasound, frequency dependent attenuation leads to decreased ARF excitation amplitude at depth, reducing SNR (Palmeri and Nightingale, 2011).

The lesion visibility metrics show similar trends to the prostate phantom analysis. In all three metrics (Figure 10A–C), mpUS and MF outperform B- mode, and mpUS outperforms SWEI ($p<0.005$). mpUS also yields a larger CNR than MF and ARFI and a larger contrast than MF ($p<0.005$). Finally, ARFI and SWEI yield an increased contrast compared to B-

Author Manuscript Author Manuscript Author Manuscript Author Manuscript

mode ($p<0.005$). As expected based upon differences in the scattering microstructure in PCa, MF outperforms B-mode in every imaging metric (Feleppa et al., 1996).

All three lesion visibility metrics are relevant in demonstrating the improvements mpUS provides over B-mode imaging alone. Contrast and CNR are indicative of how a human eye may be able to distinguish between PCa and healthy regions of the prostate. This improvement to contrast and CNR may result in an improvement in diagnostic accuracy and staging as visualization of PCa is required for targeted biopsy and is considered during disease staging. Alternatively, gCNR is more closely related to how well a computer would be able to separate the PCa from healthy prostatic tissue. As mpUS outperforms B-mode in all three visibility metrics ($p<0.005$), it is clear that mpUS would both help human readers immediately, and as we progress toward more advanced automated detection approaches in the future, mpUS would benefit artificial intelligence based readers as well.

While the analyses in this paper were performed retrospectively, creating mpUS volumes in real-time is computationally achievable. As mpUS yielded statistically significant improvements in all metrics compared to traditional TRUS B-mode, and both MF and SWEI in contrast and CNR, mpUS should be used to assess the presence of PCa. If an approach similar to this were used in the clinic, the generation of an mpUS volume could be completed in real-time which would provide an advantage over mp-MRI which requires an additional clinical visit.

Based upon these promising results, future prospective studies will be implemented using a custom designed endorectal transducer with biopsy capability paired with the Siemens Sequoia. This biopsy transducer will have elements with a larger surface area than both the Acuson ER7B and the custom Siemens 12L4 which will generate ARF excitations with greater intensity. Pairing this transducer with the Siemens Sequoia will further increase the system's capabilities as it has power supplies specifically designed to enhance ARF excitations. This increased energy output should result in better performance in the two elasticity imaging modes by improving penetration depth.

Conclusions

Using a linear SVM to create a synthetic mpUS image volume enhanced the contrast, CNR, and gCNR of PCa lesions compared to the traditional TRUS B-mode and SWEI, and led to increased contrast and CNR values compared to MF, and an increased CNR compared to ARFI. Additionally MF out performed B-mode imaging in all lesion visibility metrics, and ARFI and SWEI yielded improvements in contrast compared to B-mode as well. While ARFI only yields statistically significant differences in contrast compared to B-mode, it most clearly portrayed regional contrast, border delineation, and texture differences which are subjectively valuable for lesion detection but are not captured by the lesion visibility metrics. Although a limited retrospective study, the potential clinical value of mpUS as a method to enhance lesion visibility is demonstrated. Ongoing work will extend this process using a custom designed endorectal transducer and advanced clinical ultrasound system for prospective biopsy targeting studies.

Author Manuscript Author Manuscript Author Manuscript Author Manuscript

Acknowledgements

This work was supported by National Institutes of Health (NIH) Grants R01 CA142824, R03 EB026233, and T32-EB001040 and Department of Defense (DoD) Grant USAMRMC award number W81XWH-16-1-0653. The authors thank Siemens Medical Solutions USA, Inc., Ultrasound, for their in-kind technical support. The authors would also like to thank Anna Knight for her insights on statistical analysis.

References

Ahmed HU, El-Shater Bosaily A, Brown LC, Gabe R, Kaplan R, Parmar MK, Collaco-Moraes Y, Ward K, Hindley RG, Freeman A, Kirkham AP, Ol- droyd R, Parker C, Emberton M. Diagnostic accuracy of multi-parametric MRI and TRUS biopsy in prostate cancer (PROMIS): a paired validating confirmatory study. The Lancet, 2017;389:815–822.

Barr RG, Memo R, Schaub CR. Shear wave ultrasound elastography of the prostate: Initial results. Ultrasound Quarterly, 2012;28:13–20. [PubMed: 22357224]

Byram B, Trahey G, Palmeri M. Bayesian speckle tracking. Part II: Biased ultrasound displacement estimation. IEEE Transactions on Ultrasonics, Ferroelectrics, and Frequency Control, 2013;60:144–157.

Chan DY, Lipman SL, Palmeri ML, Morris DC, Polascik TJ, Rouze NC, Nightingale KR. Prostate Shear Wave Elastography: Multiresolution Reconstruction Dependence on Push Beam Spacing In: IEEE International Ultrasonics Symposium, IUS. Vol. 2018-January IEEE Computer Society, 2018.

Dickinson L, Ahmed HU, Allen C, Barentsz JO, Carey B, Futterer JJ, Hei- jmink SW, Hoskin PJ, Kirkham A, Padhani AR, Persad R, Puech P, Pun- wani S, Sohaib AS, Tombal B, Villers A, Van Der Meulen J, Emberton M. Magnetic resonance imaging for the detection, localisation, and characterisation of prostate cancer: Recommendations from a European consensus meeting. European Urology, 2011;59:477–494. [PubMed: 21195536]

Doherty JR, Trahey GE, Nightingale KR, Palmeri ML. Acoustic radiation force elasticity imaging in diagnostic ultrasound. IEEE Transactions on Ultrasonics, Ferroelectrics, and Frequency Control, 2013;60:685–701.

Elabbady AA, Khedr MM. Extended 12-core prostate biopsy increases both the detection of prostate cancer and the accuracy of gleason score. European Urology, 2006;49:49–53. [PubMed: 16314035]

Epstein JI, Zelefsky MJ, Sjoberg DD, Nelson JB, Egevad L, Magi-Galluzzi C, Vickers AJ, Parwani AV, Reuter VE, Fine SW, Eastham JA, Wiklund P, Han M, Reddy CA, Ciezki JP, Nyberg T, Klein EA. A Contemporary Prostate Cancer Grading System: A Validated Alternative to the Gleason Score. European Urology, 2016;69:428–435. [PubMed: 26166626]

Fedorov A, Beichel R, Kalpathy-Cramer J, Finet J, Fillion-Robin JC, Pujol S, Bauer C, Jennings D, Fennessy F, Sonka M, Buatti J, Aylward S, Miller JV, Pieper S, Kikinis R. 3D Slicer as an image computing platform for the Quantitative Imaging Network. Magnetic Resonance Imaging, 2012;30:1323–1341. [PubMed: 22770690]

Feleppa E, Kalisz A, Sokil-Melgar JB, Lizzi FL, Liu T, Rosado AL, Shao MC, Fair WR, Wang Y, Cookson MS, Reuter VE, Heston WD. Typing of prostate tissue by ultrasonic spectrum analysis. IEEE Transactions on Ultrasonics, Ferroelectrics, and Frequency Control, 1996;43:609–619.

Feleppa EJ, Mamou J, Porter CR, MacHi J. Quantitative ultrasound in cancer imaging. Seminars in Oncology, 2011;38:136–150. [PubMed: 21362522]

Halpern EJ. Contrast-enhanced ultrasound imaging of prostate cancer. Reviews in urology, 2006;8 Suppl 1:S29–S37. [PubMed: 17021624]

Heijmink SW, Futterer JJ, Strum SS, Oyen WJ, Frauscher F, Witjes JA, Barentsz JO. State-of-the-art uroradiologic imaging in the diagnosis of prostate cancer. Acta Oncologica, 2011;50:25–38.

Lipman SL, Rouze NC, Palmeri ML, Nightingale KR. Evaluating the improvement in shear wave speed image quality using multidimensional directional filters in the presence of reflection artifacts. IEEE Transactions on Ultrasonics, Ferroelectrics, and Frequency Control, 2016;63:1049–1063.

Lizzi FL, Greenebaum M, Feleppa EJ, Elbaum M, Coleman DJ. Theoretical framework for spectrum analysis in ultrasonic tissue characterization. Journal of the Acoustical Society of America, 1983;73:1366–1373. [PubMed: 6853848]

Author Manuscript Author Manuscript Author Manuscript Author Manuscript

Loupas T, Peterson RB, Gill RW. Experimental Evaluation of Velocity and Power Estimation for Ultrasound Blood Flow Imaging, by Means of a Two-Dimensional Autocorrelation Approach. IEEE Transactions on Ultrasonics, Ferroelectrics, and Frequency Control, 1995;42:689–699.

Manduca A, Lake DS, Kruse SA, Ehman RL. Spatio-temporal directional filtering for improved inversion of MR elastography images. Medical Image Analysis, 2003;7:465–473. [PubMed: 14561551]

Mottet N, Bellmunt J, Bolla M, Briers E, Cumberbatch MG, De Santis M, Fossati N, Gross T, Henry AM, Joniau S, Lam TB, Mason MD, Matveev VB, Moldovan PC, van den Bergh RC, Van den Broeck T, van der Poel HG, van der Kwast TH, Rouviere O, Schoots IG, Wiegel T, Cornford P. EAU-ESTRO-SIOG Guidelines on Prostate Cancer. Part 1: Screening, Diagnosis, and Local Treatment with Curative Intent. European Urology, 2017;71:618–629. [PubMed: 27568654]

Oelze ML, Mamou J. Review of Quantitative Ultrasound: Envelope Statistics and Backscatter Coefficient Imaging and Contributions to Diagnostic Ultrasound, 2016.

Palmeri ML, Glass TJ, Miller ZA, Rosenzweig SJ, Buck A, Polascik TJ, Gupta RT, Brown AF, Madden J, Nightingale KR. Identifying Clinically Significant Prostate Cancers using 3-D In Vivo Acoustic Radiation Force Impulse Imaging with Whole-Mount Histology Validation. Ultrasound in Medicine and Biology, 2016;42:1251–1262. [PubMed: 26947445]

Palmeri ML, Miller ZA, Glass TJ, Garcia-Reyes K, Gupta RT, Rosenzweig SJ, Kauffman C, Polascik TJ, Buck A, Kulbacki E, Madden J, Lipman SL, Rouze NC, Nightingale KR. B-mode and acoustic radiation force impulse (ARFI) imaging of prostate zonal anatomy: Comparison with 3T T2-weighted MR imaging. Ultrasonic Imaging, 2015;37:22–41. [PubMed: 25060914]

Palmeri ML, Nightingale KR. Acoustic radiation force-based elasticity imaging methods. Interface Focus, 2011;1:553–564. [PubMed: 22419986]

Patterson MS, Foster FS. The Improvement and Quantitative Assessment of B-Mode Images Produced by an Annular Array/Cone Hybrid. Ultrasonic Imaging, 1983;5:195–213. [PubMed: 6356553]

Pedregosa F, Varoquaux G, Gramfort A, Michel V, Thirion B, Grisel O, Blondel M, Prettenhofer P, Weiss R, Dubourg V, Vanderplas J, Passos A, Cournapeau D, Brucher M, Perrot M, Duchesnay E. Scikit-learn: Machine Learning in Python. Journal of Machine Learning Research, 2011;12:2825–2830.

Postema A, Mischi M, de la Rosette J, Wijkstra H. Multiparametric ultrasound in the detection of prostate cancer: a systematic review. World Journal of Urology, 2015;33:1651–1659. [PubMed: 25761736]

Postema AW, Frinking PJ, Smeenge M, De Reijke TM, De La Rosette JJ, Tranquart F, Wijkstra H. Dynamic contrast-enhanced ultrasound parametric imaging for the detection of prostate cancer. BJU International, 2016;117:598–603. [PubMed: 25754526]

Rodriguez-Molares A, Rindal OMH, D'Hooge J, Masoy SE, Austeng A, Lediju Bell MA, Torp H. The Generalized Contrast-to-Noise Ratio: A Formal Definition for Lesion Detectability. IEEE Transactions on Ultrasonics, Ferroelectrics, and Frequency Control, 2020;67:745–759.

Rohrbach D, Wodlinger B, Wen J, Mamou J, Feleppa E. High-Frequency Quantitative Ultrasound for Imaging Prostate Cancer Using a Novel MicroUltrasound Scanner. Ultrasound in Medicine and Biology, 2018;44:1341–1354. [PubMed: 29627083]

Rosenzweig S, Palmeri M, Nightingale K. Analysis of rapid multi-focal-zone ARFI imaging. IEEE Transactions on Ultrasonics, Ferroelectrics, and Frequency Control, 2015;62:280–289.

Rosenzweig S, Palmeri M, Rouze N, Lipman S, Kulbacki E, Madden J, Po- lascik T, Nightingale K. Comparison of concurrently acquired in vivo 3D ARFI and SWEI images of the prostate. In: IEEE International Ultrasonics Symposium, IUS, 2012 pp. 97–100.

Rouviere O, Melodelima C, Hoang Dinh A, Bratan F, Pagnoux G, Sanzalone T, Crouzet S, Colombel M, Mege-Lechevallier F, Souchon R. Stiffness of benign and malignant prostate tissue measured by shear-wave elastogra- phy: a preliminary study. European Radiology, 2017;27:1858–1866. [PubMed: 27553936]

Siddiqui MM, Rais-Bahrami S, Turkbey B, George AK, Rothwax J, Shakir N, Okoro C, Raskolnikov D, Parnes HL, Linehan WM, Merino MJ, Simon RM, Choyke PL, Wood BJ, Pinto PA. Comparison of MR/ultrasound fusion-guided biopsy with ultrasound-guided biopsy for the

Author Manuscript Author Manuscript Author Manuscript Author Manuscript

diagnosis of prostate cancer. JAMA - Journal of the American Medical Association, 2015;313:390–397. [PubMed: 25626035]

Siegel RL, Miller KD, Jemal A. Cancer statistics, 2020. CA: A Cancer Journal for Clinicians, 2020;70:7–30. [PubMed: 31912902]

Smith SW, Lopez H, Bodine WJ. Frequency independent ultrasound contrast-detail analysis. Ultrasound in Medicine & Biology, 1985;11:467–477. [PubMed: 3901461]

Song P, Manduca A, Zhao H, Urban MW, Greenleaf JF, Chen S. Fast shear compounding using robust 2-d shear wave speed calculation and multidirectional filtering. Ultrasound in Medicine and Biology, 2014;40:1343–1355. [PubMed: 24613636]

Walker WF, Trahey GE. A Fundamental Limit on Delay Estimation Using Partially Correlated Speckle Signals. Tech. Rep 2, 1995.

Wei C, Li C, Szewczyk-Bieda M, Upreti D, Lang S, Huang Z, Nabi G. Performance Characteristics of Transrectal Shear Wave Elastography Imaging in the Evaluation of Clinically Localized Prostate Cancer: A Prospective Study. Journal of Urology, 2018;200:549–558. [PubMed: 29605444]

Weinreb JC, Barentsz JO, Choyke PL, Cornud F, Haider MA, Macura KJ, Margolis D, Schnall MD, Shtern F, Tempany CM, Thoeny HC, Verma S. PI-RADS Prostate Imaging - Reporting and Data System: 2015, Version 2. European Urology, 2016;69:16–40. [PubMed: 26427566]

Yao LX, Zagzebski JA, Madsen EL. Backscatter Coefficient Measurements Using a Reference Phantom to Extract Depth-Dependent Instrumentation Factors. Ultrasonic Imaging, 1990;12:58–70. [PubMed: 2184569]

Author Manuscript Author Manuscript Author Manuscript Author Manuscript

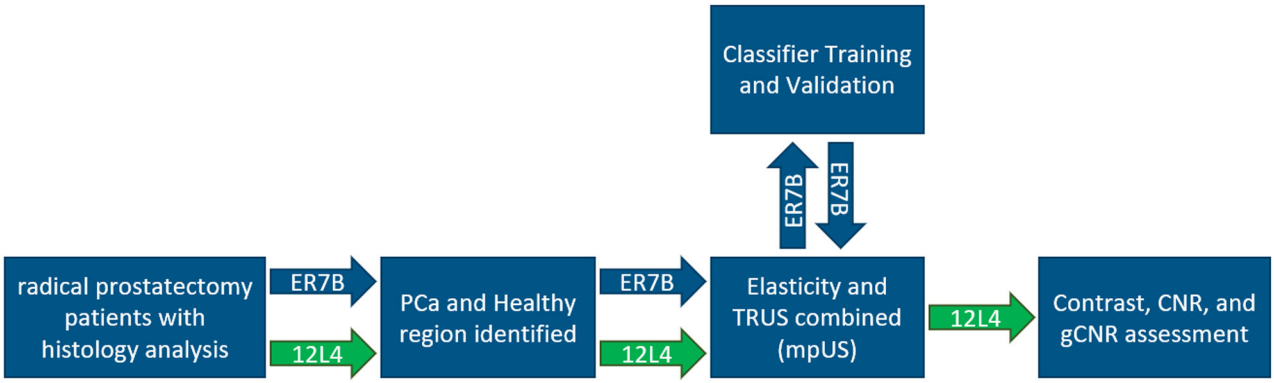

Figure 1:

This flow chart depicts the difference in the analysis between the 20 patients imaged with the ER7B (blue arrows) and the 15 patients imaged with the 12L4 (green arrows). The 20 ER7B patients were used to establish a PCa classification system which was then applied and assessed in the 15 12L4 patients.

Author Manuscript Author Manuscript Author Manuscript Author Manuscript

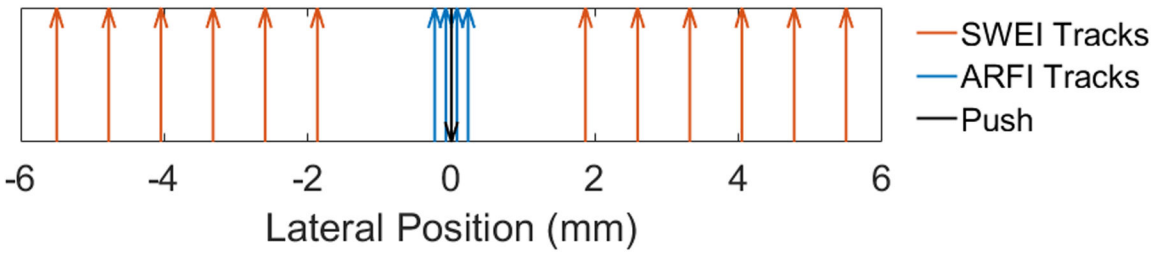

Figure 2:

Diagram of the ARFI and SWEI tracking beams relative to the ARF excitation. The ARFI tracking beams are located 0.17 mm apart centered on the ARF excitation. The 12 SWEI tracking beams are split into 6 beams per side and offset from the ARFI beams by 2.01 mm and spaced every 0.78 mm from each other.

Author Manuscript Author Manuscript Author Manuscript Author Manuscript

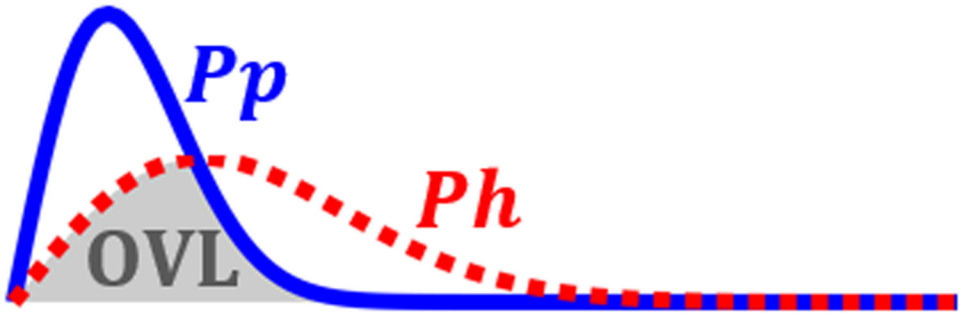

Figure 3:

Sample probability distributions for the PCa (P_p) and the healthy (P_h) tissue. The overlapping portion (gray OVL) is subtracted from 1 to calculate the gCNR.

Author Manuscript Author Manuscript Author Manuscript Author Manuscript

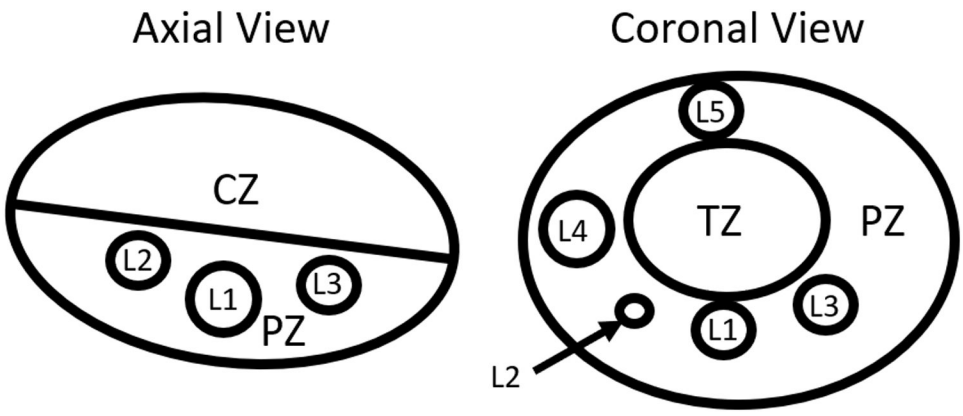

Figure 4:
Drawing of the prostate phantom defining the PZ, CZ, TZ, and lesions L1-L5. Lesion 6 is not visible in these two views of the phantom. The specific material characteristics are included in Table 4.

Author Manuscript Author Manuscript Author Manuscript Author Manuscript

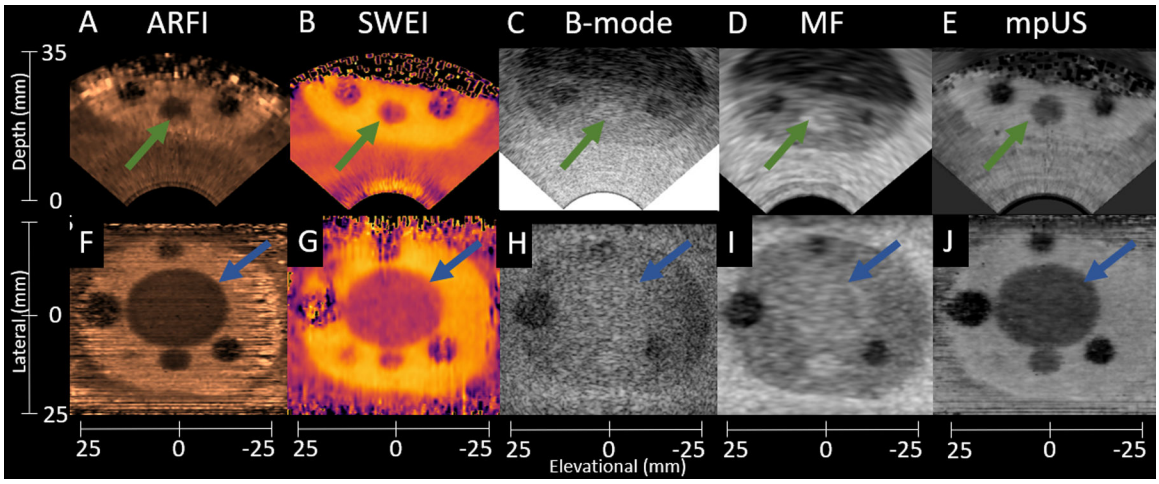

Figure 5:

Sample axial (A-E) and coronal (F-J) phantom images demonstrating the differences in lesion visibility among ARFI (A,F), SWEI (B,G), B-mode (C,H), MF (D,I), and mpUS (E,J). Lesion 1 is indicated with the green arrows, and the TZ is indicated by the blue arrows. Note the decreased lesion visibility in the B-mode images as compared to all other modalities. Also note the poorer image quality of ARFI and SWEI at increased depth axially, which occurs due to the lower SNR and poor tracking in the hypoechoic deep regions. The ARFI colormap ranges from 0.5 (black) to 5.5 (light copper). The SWEI colormap ranges from 2.0 m/s (light yellow) to 6.7 m/s (black). The B- mode colormap ranges from 0.0 dB (light gray) to −50.0 dB (black). The MF colormap ranges from 22.5 dB/m/sr (light gray) to −8.9 dB/m/sr (black). The mpUS colormap ranges from −20.0 a.u. (light gray) to 0.0 a.u. (black).

Author Manuscript Author Manuscript Author Manuscript Author Manuscript

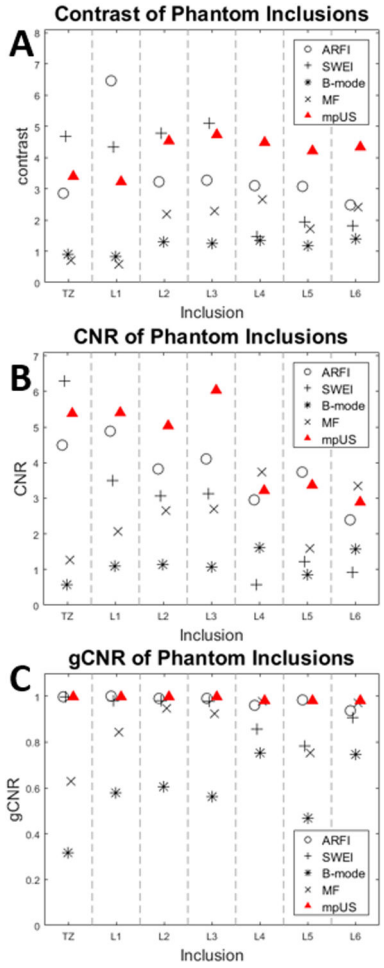

Figure 6:

Imaging metrics and imaging modality versus phantom inclusion. mpUS (red Triangle) performs consistently well across contrast (A), CNR (B), and gCNR (C). Note that in subfigure A, the B-mode (*) and MF (x) contrast for the TZ and Lesion 1 are below 1 which leads to a decrease in mpUS for these regions.

Author Manuscript Author Manuscript Author Manuscript Author Manuscript

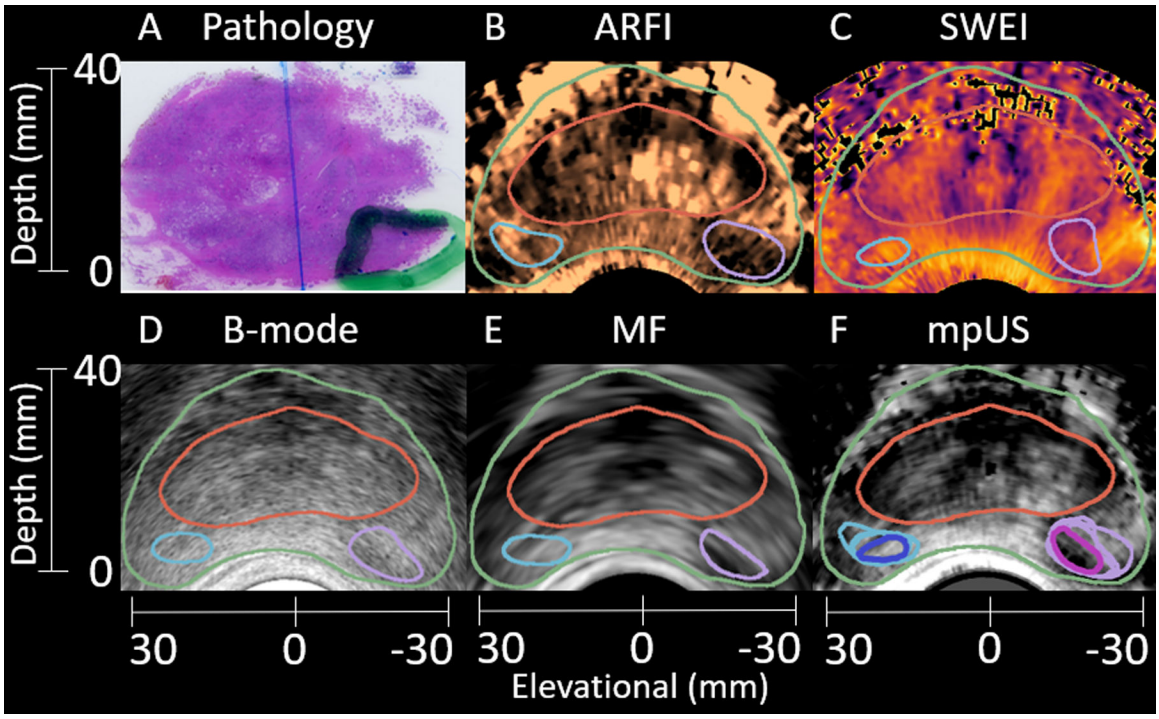

Figure 7:

Sample matched histology slide (A) with axial patient images (B-F) demonstrating identification of a clinically significant 4.2 mL Gleason Grade Group 4 (Gleason Score 4+4=8) lesion. The lesion (A, green outline) is segmented in ARFI (B), SWEI (C), B-mode (D), and MF (E) (purple outline). Another region, corresponding to healthy tissue is identified in B-E (light blue outline). The mpUS image (F) includes all segmentations with the healthy intersection (dark blue) and PCa intersection (pink). The prostate capsule (green) and CZ (red) are identified in B-F. The ARFI colormap ranges from 0.3 μm (black) to 2.9 μm (light copper). The SWEI colormap ranges from 1.1 m/s (light yellow) to 10.0 m/s (black). The B-mode colormap ranges from 0.0 dB (light gray) to −70.0 dB (black). The MF colormap ranges from 34.3 dB/m/sr (light gray) to 0.4 dB/m/sr (black). The mpUS colormap ranges from −9.0 a.u. (light gray) to 0.8 a.u. (black).

Author Manuscript Author Manuscript Author Manuscript Author Manuscript

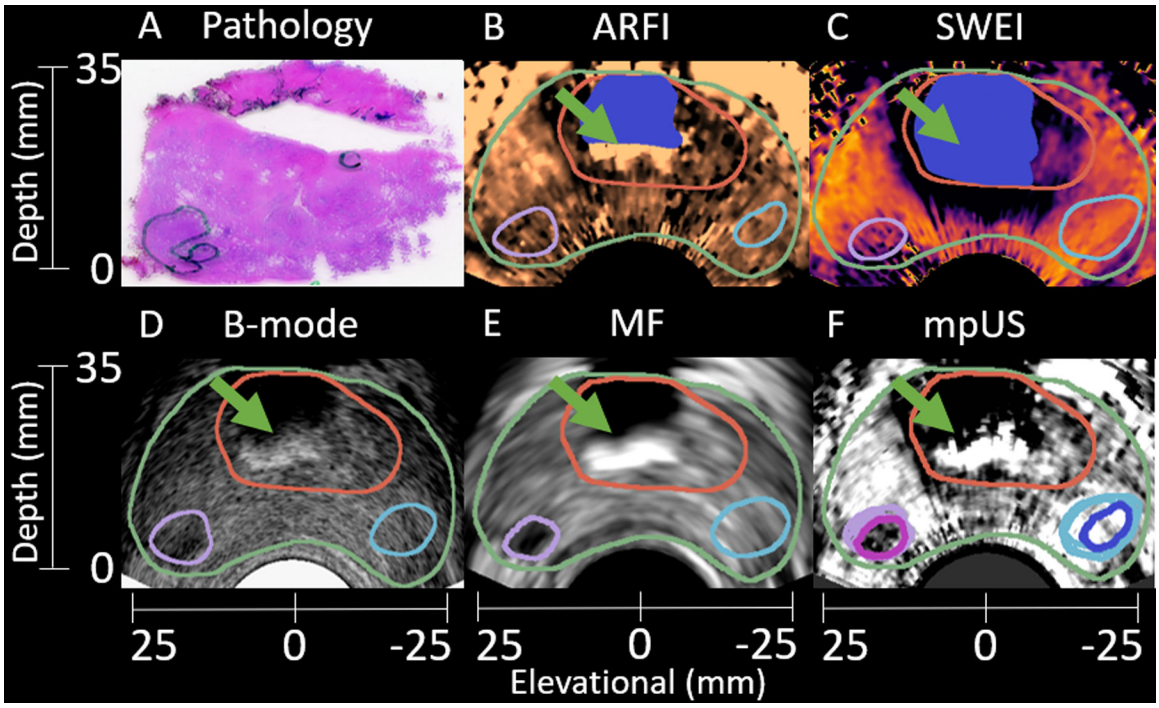

Figure 8:

Sample matched histology slide (A) with axial patient images (B-F) demonstrating identification of a clinically significant 1.0 mL Gleason Grade Group 3 (Gleason Score 4+3=7) lesion. The lesion (A, green outline) is segmented in ARFI (B), SWEI (C), B-mode (D), and MF (E) (purple outline). Another region, corresponding to healthy tissue is identified in B-E (light blue outline). The mpUS image (F) includes all segmentations with the healthy intersection (dark blue) and PCa intersection (pink). The prostate capsule (green) and CZ (red) are identified in B-F. Note the presence of calcifications in the B-mode image (green arrows). These calcifications appear as bright followed by a region of low confidence in ARFI (B), B-mode (D), MF (E) and mpUS (F) but appear dark in SWEI due to a lack of signal. A mask is applied (blue) to the ARFI and SWEI images to remove the regions of low confidence. The ARFI colormap ranges from 1.1 μm (black) to 3.5 μm (light copper). The SWEI colormap ranges from 0.8 m/s (light yellow) to 6.2 m/s (black). The B-mode colormap ranges from 0.0 dB (light gray) to −48.6 dB (black). The MF colormap ranges from 20.0 dB/m/sr (light gray) to 3.7 dB/m/sr (black). The mpUS colormap ranges from −5.0 a.u. (light gray) to −0.7 a.u. (black).

Author Manuscript Author Manuscript Author Manuscript Author Manuscript

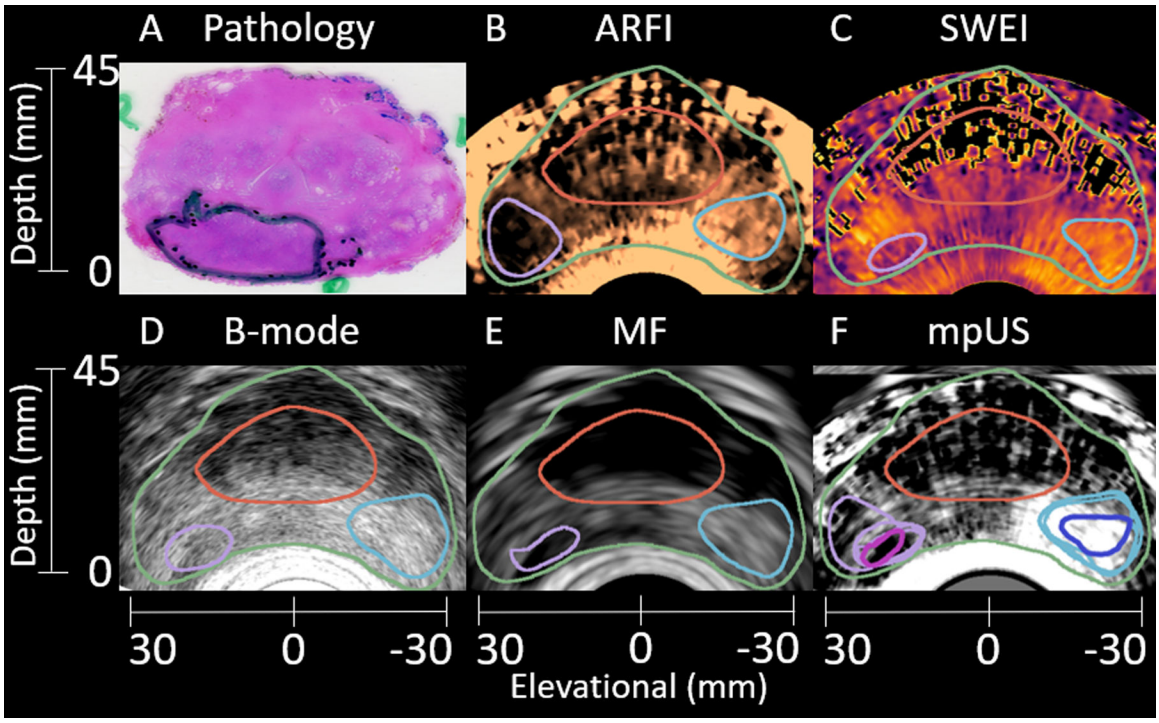

Figure 9:

Sample matched histology slide (A) with axial patient images (B-F) demonstrating identification of a clinically significant 5.3 mL Gleason Grade Group 2 (Gleason Score 3+4=7) lesion. The lesion (A, green outline) is segmented in ARFI (B), SWEI (C), B-mode (D), and MF (E) (purple outline). Another region, corresponding to healthy tissue is identified in B-E (light blue outline). The mpUS image (F) includes all segmentations with the healthy intersection (dark blue) and PCa intersection (pink). The prostate capsule (green) and CZ (red) are identified in B-F. Note the differences in shape of the PCa based on the imaging modality, and the decreased signal quality at depth in SWEI (C). The ARFI colormap ranges from 0.3 μm (black) to 3.2 μm (light copper). The SWEI colormap ranges from 2.2 m/s (light yellow) to 9.9 m/s (black). The B-mode colormap ranges from −15.3 dB (light gray) to −61.8 dB (black). The MF colormap ranges from 30.6 dB/m/sr (light gray) to 2.6 dB/m/sr (black). The mpUS colormap ranges from −4.8 a.u. (light gray) to 1.0 a.u. (black).

Author Manuscript Author Manuscript Author Manuscript Author Manuscript

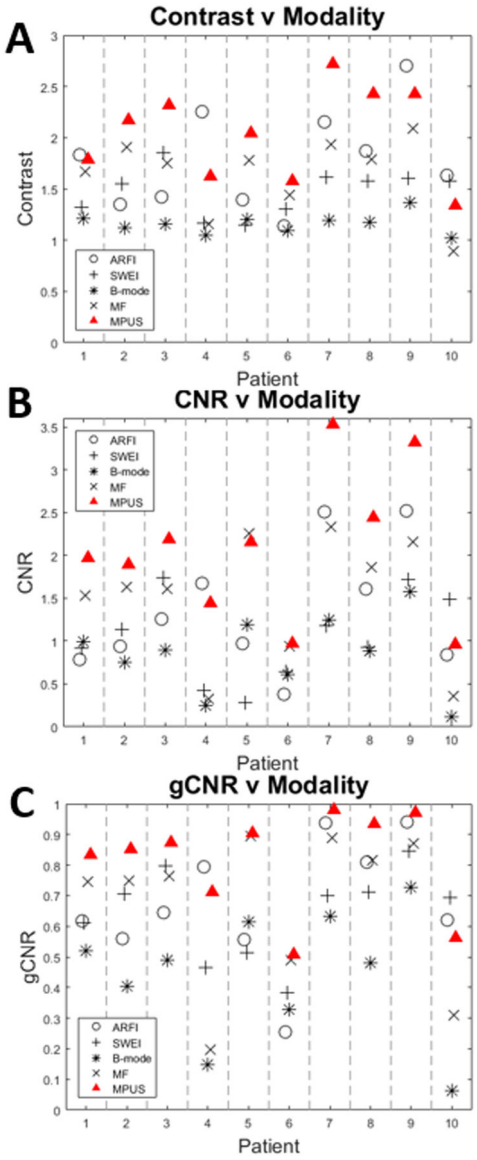

Figure 10:

Imaging metrics versus modality for each of the 10 12L4 patients. mpUS (red Triangle) performs consistently well across contrast (A), CNR (B), and gCNR (C). Note that MF (*x*) outperforms B-mode (*) in all patients and all metrics, with one exception in contrast for patient 10. Statistical analyses of these data are provided in Tables 7–9.

Author Manuscript

Author Manuscript

Author Manuscript

Author Manuscript

Table 1:

The ARF push excitation parameters for the ER7B and 12L4 transducers.

Transducer	Transmit Foci (mm)	Frequency (MHz)	Number of Cycles	F-number	Mechanical Index	Number of patients
ER7B	30, 22.5, 15	4.6, 4.6, 5.4	300, 300, 300	2.0, 2.0, 2.35	1.09, 1.39, 1.74	20
12L4	30, 22.5, 15	4.6, 4.6, 4.6	300, 300, 300	2.0, 2.0, 2.0	0.80, 1.09, 1.18	15

Author Manuscript

Author Manuscript

Author Manuscript

Author Manuscript

Table 2:

The ARFI/SWEI hybrid tracking configuration for the ER7B and 12L4 transducers.

Transducer	Transmit Focus (mm)	Frequency (MHz)	F-number	PRF (kHz)	ARFI Track Spacing (mm)	SWEI Track Offset (mm)	SWEI Track Spacing (mm)	Track Duration (ms)
ER7B	60	5.0	3.0	8.0	0.17	1.89	0.76	5
12L4	60	5.0	2.0	10.0	0.17	2.01	0.78	4.3

Author Manuscript

Author Manuscript

Author Manuscript

Author Manuscript

Table 3:

Gleason Grade Groups of PCa in ER7B and 12L4 patients.

Gleason Grade Group	ER7B (training)	12L4 (test)
1	1	0
2	5	4
3	12	3
4	1	2
5	1	0

Author Manuscript

Author Manuscript

Author Manuscript

Author Manuscript

Table 4:

Prostate Phantom Specifications.

Region	B-mode Contrast	Young's Modulus (kPa)	Lesion Diameter (mm)
PZ	1.0	20 ± 5	
TZ	0.71	45 ± 5	20
CZ	1.41	110 ± 10	
Lesion 1	0.5	75 ± 8	5
Lesion 2	1.41	75 ± 8	5
Lesion 3	1.41	110 ± 10	5
Lesion 4	1.41	110 ± 10	10
Lesion 5	1.41	110 ± 10	5
Lesion 6	1.41	110 ± 10	10

Author Manuscript

Author Manuscript

Author Manuscript

Author Manuscript

Table 5:

Lesion visibility metrics (mean ± std) for training data from 15 patients.

Modality	Contrast	CNR	gCNR
ARFI	2.9 ± 1.8	2.0 ± 1.0	0.78 ± 0.20
SWEI	2.8 ± 1.1	1.7 ± 0.8	0.75 ± 0.23
MF	2.2 ± 0.8	2.0 ± 1.0	0.79 ± 0.24
B-mode	1.2 ± 0.1	1.1 ± 0.7	0.55 ± 0.25

Author Manuscript

Author Manuscript

Author Manuscript

Author Manuscript

Table 6:

Classifier validation (mean ± std).

Classifier	Contrast	CNR	gCNR
LDA	2.40 ± 0.80	3.07 ± 1.28	0.91 ± 0.18
Linear SVM	2.40 ± 0.78	3.08 ± 1.24	0.90 ± 0.18
Decision Tree	2.08 ± 0.49	2.82 ± 1.20	0.87 ± 0.19
Random Forest	2.16 ± 0.51	3.10 ± 1.25	0.90 ± 0.20

Author Manuscript

Author Manuscript

Author Manuscript

Author Manuscript

Table 7:

Two-way Repeated Measures ANOVA.

Source	DF	F Ratio	Prob > F
Metric	2	102.91	<0.0001*
Modality	4	24.27	<0.0001*
Metric *x* Modality	8	3.03	0.0037*

*Statistically Significant Effects.

Author Manuscript

Author Manuscript

Author Manuscript

Author Manuscript

Table 8:

Repeated Measures ANOVA for each lesion visibility metric.

Metric	Source	DF	F Ratio	Prob > F
Contrast	Modality	4	13.15	<0.0001 *
CNR	Modality	4	11.17	<0.0001 *
gCNR	Modality	4	10.67	<0.0001 *

* Statistically Significant Effects

Author Manuscript Author Manuscript Author Manuscript Author Manuscript

Table 9:

P-values from Paired T-tests.

		B-mode	MF	SWEI	mpUS
ARFI	Contrast	**0.0017** *	0.4545	0.0971	0.1460
	CNR	0.0308	0.5425	0.2205	**0.0007** *
	gCNR	0.0120	0.9898	0.5686	0.0165
B-mode	Contrast		**0.0006** *	**0.0020** *	**4.75E-5** *
	CNR		**0.0003** *	0.3305	**4.13E-5** *
	gCNR		**2.18E-5** *	0.0115	**4.20E-6** *
MF	Contrast			0.1850	**0.0002** *
	CNR			0.1169	**0.0028** *
	gCNR			0.6801	0.0147
SWEI	Contrast				**0.0010** *
	CNR				**0.0034** *
	gCNR				**0.0039** *

*Statistically Significant Effects (Bonferroni corrected p<0.005).